Journal of Electronic Imaging

SPIEDigitalLibrary.org/jei

Compensating specular highlights for non-Lambertian projection surfaces

Chen-Tai Kao
Tai-Hsiang Huang
Hua Lee
Homer H. Chen

Compensating specular highlights for non-Lambertian projection surfaces

Chen-Tai Kao
Tai-Hsiang Huang
National Taiwan University
Graduate Institute of Communication Engineering
Taipei, Taiwan

Hua Lee
University of California
Department of Electrical and Computer Engineering
Santa Barbara, California

Homer H. Chen
National Taiwan University
Graduate Institute of Communication Engineering
Taipei, Taiwan
E-mail: homer@cc.ee.ntu.edu.tw

Abstract. *This paper concerns the compensation of specular highlight for handheld image projectors. By employing a projector-camera configuration, where the camera is aligned with the viewer, the distortion caused by nonideal (e.g., colored, reflective) projection surfaces can be estimated from the captured image and compensated for accordingly to improve the projection quality. This works fine when the viewing direction relative to the system is fixed. However, the compensation becomes inaccurate when this condition changes, because the position of the specular highlight changes as well. We propose a novel method that, without moving the camera, can estimate the specular highlight seen from any position and integrate it with Grossberg's radiometric compensation framework to demonstrate how view-dependent compensation can be achieved. Extensive results, both objective and subjective, are provided to demonstrate the performance of the proposed algorithm. © 2013 SPIE and IS&T [DOI: 10.1117/1.JEI.22.1.011004]*

1 Introduction

Using an image projector in a mobile phone or digital camera greatly overcomes the screen-size limitation of the handheld device and allows the image to be conveniently projected onto a bigger area on any nearby surface, such as a wall. Ideally, we would like the handheld projector to be able to project a clear image regardless of the physical characteristics of the projection surface. In practice, however, the projection surface available in the surroundings is often far from ideal and causes distortions to the projected image. As a result, geometric warping and radiometric compensation must be applied to the image before projection to counteract the nonideal characteristics of the projection surface. This compensation operation is especially important for immersive displays[1–3] and other related applications, where it is practically difficult to acquire an ideal screen. In general, algorithms for such visual computing utilize a projector-camera (procam) system, in which a number of calibration images are projected in advance, and the camera's feedback is analyzed to rectify the geometric[4–10] and photometric[11–24] properties of the projection surface. This paper concerns the radiometric compensation of a procam system.

A highly desirable technique to combat the effect of color distortion is tone mapping. It shifts the original image's color space such that, when projected on a colored screen, the compensated image is perceived undistorted. Grossberg et al.[21] proposed a procam model with a simple tone mapping. Only six calibration images are required to recover the screen's spectral response, prior to online compensation of each input image. While the chroma of the projected image is corrected, the contrast is inevitably reduced since the light absorbed by the screen is unrecoverable. Huang et al.[11] proposed to optimize the offset between chroma correctness and contrast such that radiometric compensation can be applied to deeply colored screen. Some other algorithms consider content-dependent compensation[25–27] or optimal tone mapping that is adaptive to the projector's gamut.[28,29] A detailed review of existing radiometric compensation techniques can be found in Ref. 30.

It is worth noting that, while these kinds of radiometric compensation algorithms have been successful in many cases, three major limitations remain. First, their use for non-Lambertian screens has been somewhat limited. The reason lies in the fact that, for reflective screens, the visual quality tends to be ruined by the specular highlight generated by the projection itself. The importance of this issue should not be neglected because it is hard to find an ideally diffusive surface to project whenever needed. To our knowledge, the

Paper 12343SS received Sep. 5, 2012; revised manuscript received Nov. 26, 2012; accepted for publication Dec. 21, 2012; published online Jan. 31, 2013.

problem of specular reflection regarding radiometric compensation has not been addressed before. Park et al. tried to eliminate specular light using multiple projectors,[31–33] but their work only estimated the position of the specular light. Without modeling specular light's intensity, Park's method is not applicable to radiometric compensation. Second, it is hard to characterize the specular light's intensity in a procam system because the bidirectional reflectance distribution function (BRDF) of the projection surface is unknown. For a procam system, the material of the projection surface cannot be determined in advance, so it is impossible to recover the BRDF from existing BRDF databases of various materials. Also, performing full measurement of the BRDF in a procam system is time-consuming and impractical for real-time usages. These obstacles make it hard to model, or even to eliminate, specular light in conventional radiometric compensation techniques. Third, one fundamental assumption of most radiometric compensation techniques is that the camera is placed where the viewer is supposed to be. This assumption is easily violated since the procam device can be placed statically while the viewer is allowed to move freely. In this scenario, the position of the specular light changes depending on the viewer's position, which nullifies the compensation calculated based on the statically placed camera. Thus, for non-Lambertian screens, one should design a more general radiometric compensation algorithm that takes the dynamics of specular highlight with respect to the viewing direction into consideration.

In this paper, we propose an algorithm for view-dependent radiometric compensation of non-Lambertian surfaces, with multifold contributions. First, it is a simple scheme that does not require additional projectors or cameras to reconstruct the BRDF of the surface—only one camera and one projector suffice. Second, it is the first that predicts the calibration images for different viewing angles from those captured at a single viewing angle, which greatly extends the capability of a procam system. Third, it introduces a feedback to estimate the specular light iteratively, which avoids over-compensation. Since the proposed method predicts the calibration images for an arbitrary viewing angle, it can be treated as a preprocessing module for existing radiometric compensation techniques. We show the effectiveness of the proposed method by integrating it with Grossberg's radiometric compensation framework,[21] which is accurate only at the viewing angle where the calibration images are captured. By predicting calibration images at various viewing angles using our method, automatic photometric compensation for an arbitrary viewing angle is made possible.

This paper is organized as follows. We introduce specular light in Sec. 2, and then we describe the proposed radiometric compensation algorithm in Sec. 3 and the experimental results in Sec. 4. Then the subjective and objective evaluations are provided in Sec. 5. Finally, the conclusions are drawn in Sec. 6.

2 Specular Highlight Modeling

Consider projection onto a non-Lambertian (or reflective) screen. While most of the light is evenly scattered, a small portion of light rays directly reflect as if the surface is a mirror. This mirror-like reflection of light is commonly known as specular highlight and has been considered important in three-dimensional (3-D) computer graphics.[34–38] There exist different models for predicting the distribution of the specular highlight, such as the Phong model,[38] the Blinn-Phong model,[37] the Gaussian distribution model,[39] and the Cook-Torrance model.[36]

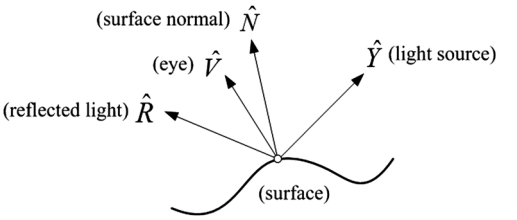

Fig. 1 Notations used in the Phong model. It characterizes how a viewer (at $\hat{V}$) perceives the reflected light (at $\hat{R}$) of an incident light (at $\hat{Y}$) on a point with surface normal $\hat{N}$.

We model the specular highlight using the Phong model and the notations shown in Fig. 1 in the following derivation. For each point on the surface, the specular light I_s is given by

$$I_s = \sum_{m \in \mathcal{L}} k_s (\hat{R}_m \cdot \hat{V})^{\gamma} i_{m,s}, \tag{1}$$

where $\mathcal{L}$ is the set of all light sources, k_s is the specular reflection constant, $\hat{R}_m$ is the direction of the perfectly reflected light, $\hat{V}$ is the direction toward the viewer, γ is the shininess constant for the screen material, and $i_{m,s}$ is the intensity of the light source. Note that $\hat{R}_m$ and $\hat{V}$ are unit vectors.

3 Proposed Approach

Figure 2 shows the overall architecture of the proposed method, which generates view-dependent compensated images for a non-Lambertian surface. The method first projects a uniform image onto the surface. Then it utilizes the projected image to fit the specular highlight model, estimate the calibration images viewed at different positions, and perform radiometric compensation using the estimated calibration images. The radiometric compensation framework proposed in Ref. 21 is adopted in our work.

To perform geometric calibration, a chessboard pattern is projected on the surface and captured by the camera. We then detect the chessboard corners in the captured image and apply Zhang's method[40] to find the geometric transformation that calibrates perspective distortion and radial distortion. Subsequently, all captured images are geometrically calibrated by the same geometric transformation.

Since the perceived specular light varies with respect to the viewing angle of a viewer, we need a precise description of the viewing angle. Assuming the viewer can only move along the xz-plane in Fig. 3, which depicts the viewing geometry, we define the viewing angle θ, measured in degree, to be 90 deg when the viewer stands right in front of the screen. In its simplest form, we assume the viewer and the procam system are at the same height. That is, the change of the viewing angle only has one degree-of-freedom. When precise spatial information of the viewer is available, the proposed method can be extended to account for 2-D variation of the viewing angle. In this section, the details of the proposed method are described in accordance with the processing flow shown in Fig. 2.

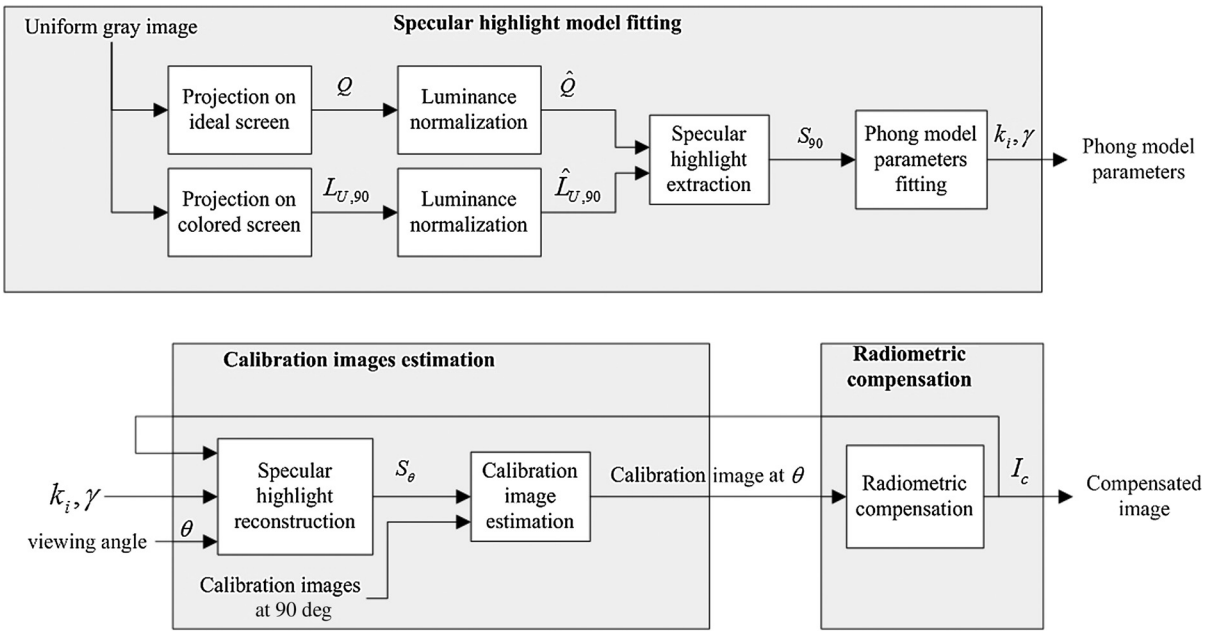

Fig. 2 The architecture of the proposed method, which consists of three major components: specular highlight model fitting, calibration images estimation, and radiometric compensation.

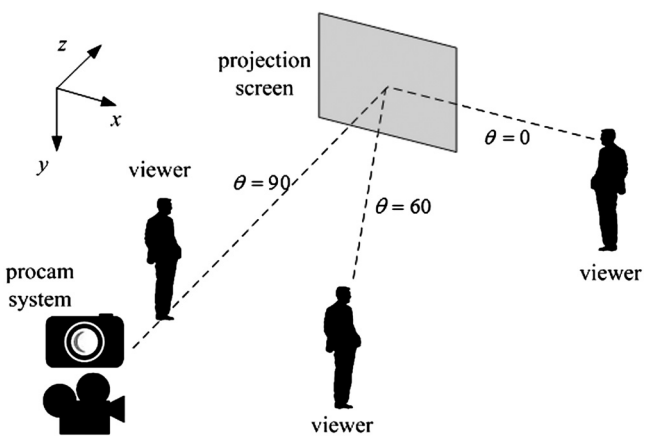

Fig. 3 The definition of viewing angle θ (measured in degree). $\theta = 90$ deg when the viewer stands right in front of the screen.

3.1 *Specular Highlight Model Fitting*

We estimate the unknown parameters, k_s, γ, and $i_{m,s}$, in the Phong model from the luminance variation of a projected image. We project a uniform gray image onto the screen and capture it by a camera placed at 90 deg. The captured image $L_{U,90}$ is normalized to $\hat{L}_{U,90}$ by

$$\hat{L}_{U,90} = \frac{L_{U,90}}{n}, \tag{2}$$

where

$$n = \max_{x,y} L_{U,90}(x,y) \tag{3}$$

is the normalizing constant. $\hat{L}_{U,90}$, with value ranging from 0 to 1, denotes the spatial variation of the luminance. Note that we cannot estimate the Phong model directly from $\hat{L}_{U,90}$, because the luminance variation is caused by the combination of the following two factors: (1) vignetting and (2) specular highlight. Vignetting, introduced by the imperfection of lens, often results in luminance reduction at the periphery of a photo. Therefore we need to estimate and exclude the vignetting factor before reconstructing the Phong model.

The vignetting effect can be calculated by projecting the same uniform gray image onto an ideal projection screen, which is assumed to be highly, if not perfectly, diffusive. More specifically, no specular light should appear on the ideal projection screen. We normalize the captured image Q to obtain $\hat{Q}$, which is the luminance variation caused by pure vignetting. Since the vignetting effect remains identical under the same procam configuration, we can extract the specular highlight S_{90} by

$$S_{90}(x,y) = \frac{\hat{L}_{U,90}(x,y)}{\hat{Q}(x,y)}. \tag{4}$$

It should be noted that the division is performed pixel-wise. The two-dimensional (2-D) specular highlight S_{90} is then sampled along then sampled along the x-axis [see Fig. 4(a)] to obtain the one-dimensional (1-D) curve of the specular highlight, as shown in Fig. 4(b). The 1-D curve, denoted by s, fully characterizes the change of the specular light along the x-axis of the captured image. Data formed by s are used as samples of I_s in Eq. (1) to estimate the unknown parameters k_s, γ, and $i_{m,s}$. In our scenario, the screen is assumed to be homogeneous, i.e., made of the same material, so one set of k_s and γ suffices. Since there is only one light source (the projector), Eq. (1) can be rewritten as

$$s(x) = k_s[\hat{R}(x,y) \cdot \hat{V}(x,y)]^{\gamma} i_s|_{y=h}, \tag{5}$$

where h is the height of the camera. Note that the value of $\hat{R}$ and $\hat{V}$ can be obtained by considering the relative position of

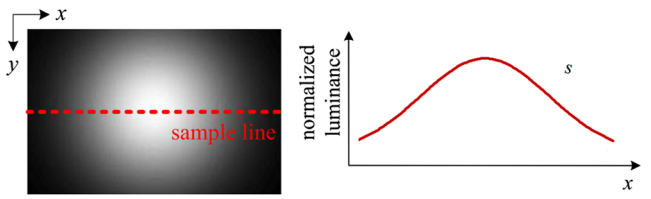

Fig. 4 (a) Specular highlight of a reflective projection surface when seen at 90 deg; (b) 1-D sample of the specular highlight.

the projector, the camera, and each point $p(x,y)$ on the projection surface. For each point $p(x,y)$ on the projection surface, $\hat{V}$ points from $p(x,y)$ toward the camera, $\hat{Y}$ points from $p(x,y)$ toward the projector, and the direct reflected light $\hat{R}$ can be computed as

$$\hat{R} = 2(\hat{Y}\cdot\hat{N})\hat{N} - \hat{Y}, \tag{6}$$

where $\hat{N}$ is the surface normal. The geometric interpretation of Eq. (6) is shown in Fig. 5(c). Note that $\hat{V}$, $\hat{R}$, $\hat{N}$, and $\hat{Y}$, are all unit vectors in 3-D space. Figure 5(a) demonstrates the camera direction for planar projection surface. With variables rearranged, and logarithm taken on both sides of Eq. (5), the equation becomes

$$\log[s(x)] = \log(k_s i_s) + \gamma \log[\hat{R}(x,y)\cdot\hat{V}(x,y)]|_{y=h}. \tag{7}$$

Based on the scatter plot of $\log(s)$ and $\log(\hat{R}\cdot\hat{V})$, we use linear regression to obtain $k_s i_s$ and γ.

The method can also be extended to use all samples in $S_{90}(x,y)$ to fit the Phong model, instead of using only the 1-D samples of s. In this case, Eq. (1) is rewritten as

$$S_{90}(x,y) = k_s[\hat{R}(x,y)\cdot\hat{V}(x,y)]^{\gamma} i_s, \tag{8}$$

and $k_s i_s$ and γ can be fitted by linear regressing all data points in $S_{90}(x,y)$. Since more samples are used, the fitted parameters may be more accurate.

3.2 *Calibration Images Estimation*

Given the specular light response of the screen at $\theta = 90$, we now move the virtual camera to an arbitrary viewing angle θ and reconstruct the 2-D specular highlight S_θ observed there. It follows from Eq. (1) that we can predict S_θ by

$$S_\theta(x,y) = k_s[\hat{R}(x,y)\cdot\hat{V}_\theta(x,y)]^{\gamma} i_i, \tag{9}$$

where $\hat{V}_\theta(x,y)$ denotes the direction pointing from the pixel $p(x,y)$ to the virtual camera at viewing angle θ. Note that k_i, i_i, and γ are as computed in Sec. 3.1, and $\hat{R}$ remains unchanged because the projector stays at the same place. Figure 5(b) demonstrates how the values of $\hat{V}_\theta(x,y)$ and $\hat{R}(x,y)$ can be obtained.

Five calibration images should be captured ($L_{R,\theta}$, $L_{G,\theta}$, $L_{B,\theta}$, $L_{U,\theta}$, and $L_{S,\theta}$) for the radiometric compensation framework (see Sec. 3.3). To generate radiometric compensation for viewing angle θ, the calibration images at that viewing angle should be estimated. Calibration images at θ($L_{R,\theta}$, $L_{G,\theta}$, $L_{B,\theta}$, $L_{U,\theta}$, and $L_{S,\theta}$) are estimated by adding the change of specular light on the calibration images at $\theta = 90$. That is,

$$L_{M,\theta} = L_{M,90} + n(S_\theta - S_{90}), \qquad M \in \{R,G,B,U,S\}, \tag{10}$$

where n is the normalizing constant defined in Eq. (3) and θ denotes the viewing angle (measured in degree) of the calibration images.

3.3 *Radiometric Compensation*

We adopt the framework proposed in Ref. 11 for radiometric compensation, which is based on the procam model first introduced by Grossberg et al.[21] Grossberg's model has great advantage in that only six calibration images are needed for the photometric compensation. Because Grossberg's model deals with screens with spatially variant color, an "invariant value" is computed pixel-wise in order to reflect the color distortion of each pixel.[21] In our scenario, where the screen color is assumed to be spatially uniform, the computation of that "invariant value" is not needed. This saves one calibration image, and thus only five calibration images are required. These calibration images consist of

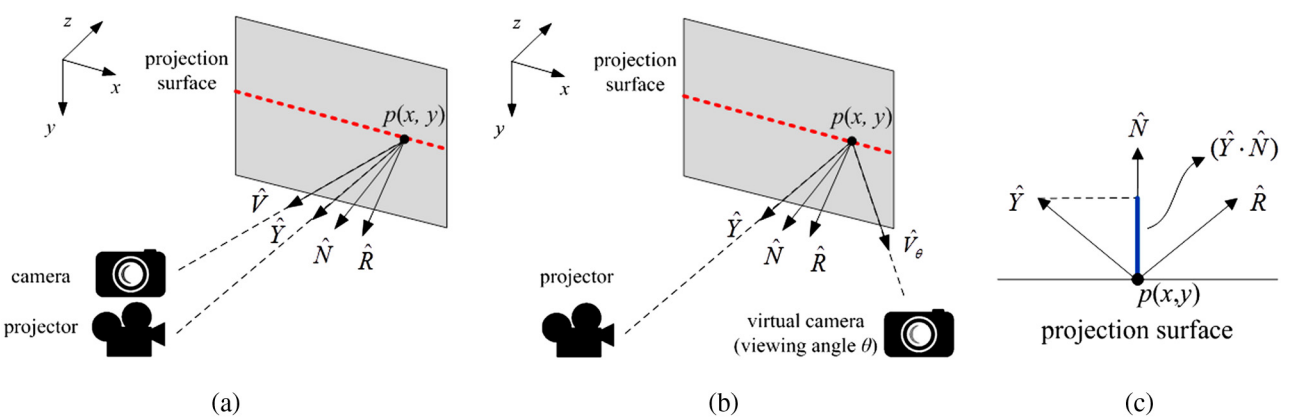

Fig. 5 Illustration of the camera direction in (a) Phong model fitting for planar projection surface and (b) specular light estimation. In the model fitting, the camera is placed right above the projector. In the specular light estimation, the virtual camera is placed at a different angle θ. In both conditions, the direct reflected light $\hat{R}$ is calculated by Eq. (6), whose geometric interpretation is shown in (c).

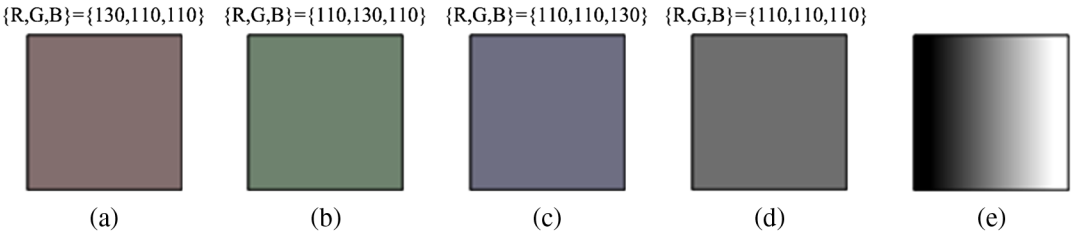

Fig. 6 The five calibration images: (a) red, (b) green, (c) blue, (d) gray, and (e) slope—a ramp with pixel values ranging from 0 to 255.

Table 1 Configuration of the five calibration images.

Color	Pixel value
Red	$\{R, G, B\} = \{130, 110, 110\}$
Green	$\{R, G, B\} = \{110, 130, 110\}$
Blue	$\{R, G, B\} = \{110, 110, 130\}$
Gray	$\{R, G, B\} = \{110, 110, 110\}$
Slope (ramp)	$\{R, G, B\} = \{0, 0, 0\} \sim \{255, 255, 255\}$

four uniform-colored images (red, green, blue, and gray) and one color ramp consisting of pixels ranging from gray-level 0 to gray-level 255 (Slope). We denote the gray image as U. These images are shown in Fig. 6(a) to 6(e), whose pixel values are summarized in Table 1. The pixel values of the four uniform-colored images should not be set too low; otherwise, the captured image may be subject to severe noise generated by the camera sensor. They should not be set too high, either, since the projector's response curve is nearly flat when displaying very bright content. Therefore, we set the pixel values to be around 110 to 130, a much safer choice near the middle of 0 to 255. We project these calibration images and denote the captured images as $L_{M,\theta}$, $M \in \{R, G, B, U, S\}$, where the camera is placed at viewing angle θ.

Here we want to emphasize a crucial contribution of the proposed method: no extra image is needed for the reconstruction of the specular highlight response. We use the gray calibration image $L_{U,90}$ as the source image to estimate the specular highlight. The brightness of U is carefully chosen such that specular light appears, while the resulting luminance variation is recordable by the camera. Empirically, the pixel value is set to 110.

The procam model is shown in Fig. 7, with each part illustrated as follows. First, the original image I, after being mapped by the projector's response curve f_p, becomes the projected luminance P,

$$P = f_p(I), \tag{11}$$

where f_p is typically a nonlinear transfer function. Note that $I = [I_r, I_g, I_b]^T$ is the input image with pixel value ranging from 0 to 255, while $P = [P_r, P_g, P_b]^T$ is in the luminance domain. Both I and P are 3-D vectors (red, green, and blue channel).

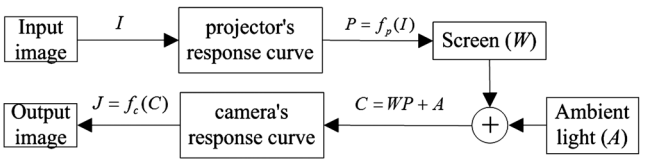

Fig. 7 Grossberg's procam model. The input image I is first mapped by the projector's response curve f_p. The projected luminance P is then modulated by the screen's color (modeled as a 3×3 color mixing matrix W) and the ambient light A before being captured by the camera. The captured luminance is then mapped by the camera's response curve f_c to be the output image J.

The overall modulation of the screen is modeled by a 3×3 matrix W that characterizes all possible interactions between the incident light and the reflected light:

$$W = \begin{bmatrix} W_{RR} & W_{RG} & W_{RB} \\ W_{GR} & W_{GG} & W_{GB} \\ W_{BR} & W_{BG} & W_{BB} \end{bmatrix}. \tag{12}$$

Generally, W is called the color mixing matrix, which captures the coupling between each color channel of the projector and the camera. W_{GR}, for example, denotes the portion of red channel of the projector that contributes to the green channel of the camera. It should be noted that W is spatially variant for each pixel in the projected screen.

By adding the ambient light A, the captured image C is modeled by

$$C = WP + A, \tag{13}$$

where C, P, and A are 3-D vectors (red, green, and blue channel), and W is as defined in Eq. (12). The captured image C is then transformed back by the camera response curve f_c to result in the output image J,

$$J = f_c(C). \tag{14}$$

Grossberg et al.,[21] proposed an efficient method to recover all parameters of the procam model. First, the color-mixing matrix W is decomposed by

$$W = \tilde{W}D = \begin{bmatrix} 1 & \tilde{W}_{RG} & \tilde{W}_{RB} \\ \tilde{W}_{GR} & 1 & \tilde{W}_{GB} \\ \tilde{W}_{BR} & \tilde{W}_{BG} & 1 \end{bmatrix} \begin{bmatrix} W_{RR} & 0 & 0 \\ 0 & W_{GG} & 0 \\ 0 & 0 & W_{BB} \end{bmatrix}, \tag{15}$$

where $\tilde{W}$ and D encodes the inter-channel and the intra-channel interaction, respectively. $\tilde{W}$ can be determined using just four calibration images ($L_{R,\theta}$, $L_{G,\theta}$, $L_{B,\theta}$, and $L_{U,\theta}$). Let

$\bar{L}_{R,\theta}$, $\bar{L}_{G,\theta}$, $\bar{L}_{B,\theta}$, $\bar{L}_{U,\theta}$ denote the mean pixel value of $L_{R,\theta}$, $L_{G,\theta}$, $L_{B,\theta}$, $L_{U,\theta}$, respectively, then $\tilde{W}$ can be computed as

$$\tilde{W} = \begin{bmatrix} 1 & \frac{\{\bar{L}_{G,\theta}-\bar{L}_{U,\theta}\}_r}{\{\bar{L}_{G,\theta}-\bar{L}_{U,\theta}\}_g} & \frac{\{\bar{L}_{B,\theta}-\bar{L}_{U,\theta}\}_r}{\{\bar{L}_{B,\theta}-\bar{L}_{U,\theta}\}_b} \\ \frac{\{\bar{L}_{R,\theta}-\bar{L}_{U,\theta}\}_g}{\{\bar{L}_{R,\theta}-\bar{L}_{U,\theta}\}_r} & 1 & \frac{\{\bar{L}_{B,\theta}-\bar{L}_{U,\theta}\}_g}{\{\bar{L}_{B,\theta}-\bar{L}_{U,\theta}\}_b} \\ \frac{\{\bar{L}_{R,\theta}-\bar{L}_{U,\theta}\}_b}{\{\bar{L}_{R,\theta}-\bar{L}_{U,\theta}\}_r} & \frac{\{\bar{L}_{G,\theta}-\bar{L}_{U,\theta}\}_b}{\{\bar{L}_{G,\theta}-\bar{L}_{U,\theta}\}_g} & 1 \end{bmatrix}, \quad (16)$$

where indices r, g and b denote the red, green and blue channels, respectively. Multiplying $\tilde{W}^{-1}$ on both sides of Eq. (13) yields

$$\tilde{C} = DP + \tilde{A}, \quad (17)$$

where

$$\tilde{C} = \tilde{W}^{-1}C, \quad (18)$$

and

$$\tilde{A} = \tilde{W}^{-1}A. \quad (19)$$

We say that Eq. (17) decouples the color response of the screen, since each color channel in $\tilde{C}$ is now affected only by the same channel of the projector, the screen and the ambient light. The monotonic mapping ρ between the pixel value (0 to 255) and the corresponding decoupled luminance is defined as

$$\tilde{C} = \rho(I). \quad (20)$$

We reconstruct ρ by the regression of $\tilde{L}_{S,90}(x,y)$, where $\tilde{L}_{S,90}(x,y) = \tilde{W}^{-1}L_{S,90}(x,y)$.

We reconstruct $\tilde{W}$ and ρ for the white screen and the colored screen, denoted by $\{\tilde{W}_w, \rho_w\}$ and $\{\tilde{W}_c, \rho_c\}$, respectively, by projecting the calibration images onto both screens. Once the parameters are reconstructed, we gain full information about how the projected image is perceived on both screens. Therefore it becomes possible to compensate the radiometric distortion and to make the projection onto a colored screen looks as if it is projected onto a white screen.

Figure 8 illustrates the radiometric compensation framework for a test image I_w. Under this framework, we generate a compensated image I_c that, when projected on the colored screen, is perceived almost the same as projection of I_w on the white screen. The test image is converted first to the decoupled luminance ($\tilde{C}_w$) by ρ_w, then to the desired luminance (C_w) by multiplying the color-mixing matrix $\tilde{W}_w$. Here C_w serves as a simulation of the perceived luminance supposing the test image is projected on the white screen.

Projection onto a colored screen often leads to loss of the dynamic range because the upper bound of displayable luminance is modulated by the screen color, while the lower bound is determined by the ambient light that brings additional luminance to black pixels (see Fig. 9). Therefore compensation toward photometric correctness requires that the dynamic range be compressed within the recoverable range. This can be achieved by tone mapping, but the image contrast is inevitably reduced. A technique was developed in Eq. (11) to optimize the tradeoff between the photometric correctness and the contrast. The tone mapping function is defined as follows:

$$C_c = \alpha C_w + \beta. \quad (21)$$

Here, α and β are determined by considering two kinds of error: over-upper-bound error (E_u) and below-lower-bound error (E_l). E_u and E_l account for pixels that, after this tone mapping, lie outside the recoverable dynamic range. In practice, E_u is computed as the sum of pixels whose luminance lies over the upper bound; E_l for pixels with luminance below the lower bound. α and β are determined by the following optimization:

$$(\alpha, \beta) = \underset{\alpha,\beta}{\operatorname{argmin}}(E_u + E_l) + \lambda E_b, \quad (22)$$

where $E_b = (1-\alpha)^2$ is the penalty term for brightness and λ is a weighting factor. The optimization attempts to maximize the number of pixels that lie within the recoverable dynamic range, while preserving as much contrast as possible.

We compute the compensated image I_c from the desired luminance C_c by decoupling the color channels, followed by mapping the decoupled luminance to an 8-bit pixel value. The following equations give the compensated image I_c:

$$\tilde{C}_c = \tilde{W}_c^{-1}C_c, \quad (23)$$

$$I_c = \rho_c^{-1}(\tilde{C}_c). \quad (24)$$

The quality of the compensated image is determined by the reconstructed parameters of the procam model, which in turn depends fully on the captured calibration images. Since the

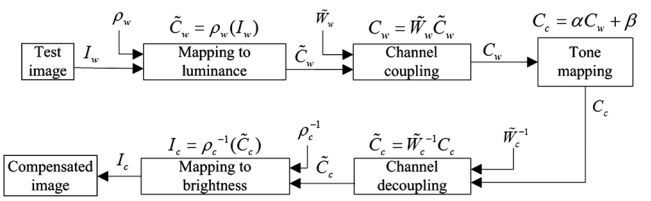

Fig. 8 The block diagram of radiometric compensation. The test image I_w is first converted to the decoupled luminance $\tilde{C}_w$, then the color-mixing-matrix $\tilde{W}_w$ is used to compute the coupled luminance C_w. The tone mapping function in Eq. (21) is used to map the luminance C_w seen on white-screen to the luminance C_c on colored-screen. Finally, the luminance is decoupled by $\tilde{W}_c^{-1}$ to be the decoupled luminance $\tilde{C}_c$, which is then converted back to the compensated image I_c.

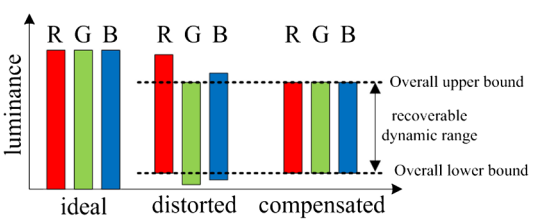

Fig. 9 When the brightest white is projected onto a colored screen, each color channel suffers from a different amount of distortion. The upper bound of each channel is independently modulated by the screen's color, while the lower bound is determined by the reflected ambient light that adds additional luminance to black pixels. Radiometric compensation recovers the color, with the recoverable dynamic range determined by the minimum dynamic range of the three channels. The contrast is therefore decreased.

calibration images are estimated by a virtual camera colocated with the viewer, the compensation is view-dependent. For simplicity, we refer to the image compensated for viewing angle θ as "θ compensated image." For example, if the viewer is at 60 deg, the compensated image is denoted by 60 deg compensated image.

3.4 *Specular Highlight Estimation Feedback*

The luminance of the projected light determines the chroma and the intensity of the specular highlight. In particular, when a compensated image is projected, the specular light slightly differs from that estimated in the initial condition, under which the calibration image is projected. This often leads to over-compensation, which is explained as follows. Suppose a green compensation image is projected onto a magenta screen, which is expected to recover a purely gray image. Due to the compensation, the projection is now much greener, making the specular light greener as well. Extra hue distortion is thus added to the originally well-compensated gray image, resulting in overcompensation.

We propose to incorporate the specular highlight estimation feedback that estimates the specular light based on the content of the compensation image. Since the new compensation image only affects the intensity of specular light (i_s) in the Phong model, we change the estimated parameter $k_s i_s$ by replacing i_s with i_c according to the following equation:

$$i_c = i_s \frac{\bar{I}_c}{\bar{U}}, \tag{25}$$

where $\bar{U}$ and $\bar{I}_c$ are the mean pixel intensity of U and I_c, respectively. Note that Eq. (25) is computed respectively for each color channel. In practice, we iterate the feedback loop three times.

Here the light from the projector is modeled as a point source. This is definitely a simplified, yet usable, model. More complex modeling can be designed to compute the projector's light field, which considers the specular light caused by each single beam projected onto each pixel on the surface. Nevertheless, this is beyond the scope of this paper and deserves a separate treatment.

3.5 *Possible Extension*

The proposed method is designed for, but not limited to, procam systems consisting of a projector and a camera bound together. This is the most applicable configuration that can be nicely packaged as one unit and is well suited for mobile projectors. For a procam system with multiple projectors and cameras, some extra work is needed for the proposed technique to be adopted. In the case of multiple projectors, geometric registration (e.g., using Zhang's method)[40] is needed for each projector to seamlessly merge all projections. Then our technique can be used to estimate the specular light contributed by each projector. Specifically, we can divide the image to be projected into a number of patches, each of which is then projected onto the projection surface by the specific projector that produces the least specular light for that patch. In this way, the system is able to support multiple viewers at different viewing angles simultaneously with minimum specular light perceived by each viewer. With multiple cameras, on the other hand, the system is able to estimate the specular light distribution more accurately, because images captured at various viewing angles now provide more samples to fit the specular light model.

4 Experimental Results

The proposed algorithm is applied to the radiometric compensation framework described in Ref. 11 and shown in Fig. 2 as the radiometric compensation module. Specifically, we integrate specular highlight model fitting and calibration images estimation with the radiometric compensation module.

Figure 10 shows the experimental setup of our procam system, which consists of a projector (SanyoPLC-XW56) and a camera (Canon40D). The screen is an A4 paper, one half of which is printed in color by a color laser printer. It should be noted that the printed ink is itself reflective, making the colored side a non-Lambertian surface. Also note that both the projector and the camera are placed at 90 deg viewing angle.

We report results for two test images, namely Waterfall and Motorbikes. The resolution of both images is 640×320. The projection of both images on the white screen is shown in Fig. 11, which serves as ideal images for other projections to compare with. We project Waterfall on a magenta screen, where the photometric distortion is shown in Fig. 12(a). To compensate for the distortion, 90 deg compensated image is projected and the result is captured by a camera placed at 90 deg [see Fig. 12(b)]. Although Fig. 12(b) recovers most visual quality, the compensation becomes inaccurate when seen at 60 deg, as shown in Fig. 12(c). In fact, the specular light present at 90 deg almost vanishes when seen from 60 deg, thus the image's chroma is subject more to the screen color. Figure 12(d) gives the projection of 60 deg compensation, in which the color is corrected by the proposed algorithm.

The effectiveness of the proposed method can be identified by examining the green color that is recovered. As a matter of fact, green is the most absorbed color for a magenta screen. Therefore, when the viewing angle changes from 90 to 60 deg, it is the green channel that is the most severely affected. By comparing the green channel that is recovered in Fig. 11(c) and 11(d), it becomes clear that the proposed method offers a satisfactory solution for retaining consistent visual quality across different viewing angles.

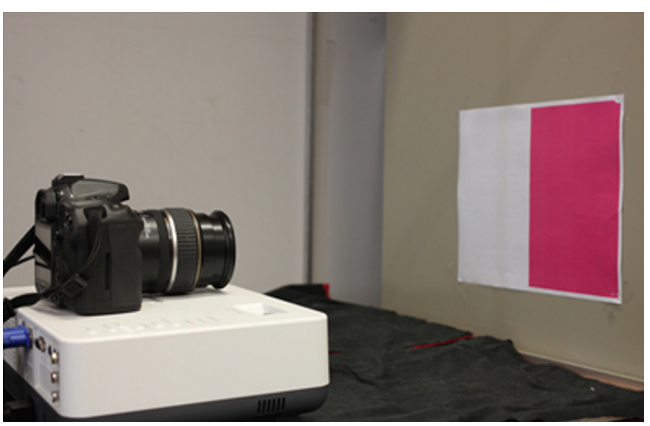

Fig. 10 Experimental setup. The procam consists of a projector (Sanyo PLC-XW56) and a camera (Canon 40D). The screen is an A4 white paper, one half of which is printed in color by a color laser printer.

(a) (b)

Fig. 11 Two test images projected on a white surface: (a) Waterfall and (b) Motorbikes.

(a) (b) (c) (d)

Fig. 12 Waterfall projected on a magenta surface and seen at different viewing angles:(a) original image seen at 90 deg; (b) 90 deg compensated image seen at 90 deg; (c) 90 deg compensated image seen at 60 deg; (d) 60 deg compensated image seen at 60 deg.

(a) (b) (c) (d)

Fig. 13 Motorbikes projected on a green surface and seen at different viewing angles: (a) original image seen at 90 deg; (b) 90 deg compensated image seen at 90 deg; (c) 90 deg compensated image seen at 60 deg; (d) 60 deg compensated image seen at 60 deg.

Figure 13 shows the result for another test image Motor bikes. In this case, a green screen is used. The implication of the result is similar to that of Fig. 12.

5 Evaluation

To validate the proposed method, an evaluation is conducted to test the model under a representative condition. The same set of 90 deg compensated and 60 deg compensated images are projected onto a reflective color surface, and the projection results are evaluated both objectively and subjectively.

5.1 *Comparison with the Ideal Image*

This section presents a quantitative analysis of the proposed method in terms of its ability of projection quality enhancement. To evaluate the method's generality, a test image is first projected on an ideal screen as the ground truth T_i. We then project the following onto the colored screen: (1) original image T_o; (2) 90 deg compensated image T_{90}; and (3) 60 deg compensated image T_{60}. To compare the visual quality seen at different viewing angle, we capture the images of T_o, T_{90}, and T_{60} at 60 deg. The quality of T_o,

Table 2 Comparison of the sum of squared error (unit: 10^7).

Screen color	Pixel value of the test image [R G B]	Seen at 90 deg			Seen at 60 deg		
		T_o	T_{90}	T_{60}	T_o	T_{90}	T_{60}
Red	[100 50 50]	8.48	**1.70**	4.23	12.4	2.74	**1.87**
	[50 100 50]	16.7	**3.73**	7.34	27.7	5.64	**3.57**
	[50 50 100]	17.8	**5.41**	7.32	27.6	9.98	**8.16**
Green	[100 50 50]	14.1	**3.82**	3.98	18.1	5.72	**1.70**
	[50 100 50]	14.1	**7.55**	7.73	18.4	9.95	**7.42**
	[50 50 100]	12.0	**6.12**	6.71	14.3	7.55	**4.76**
Blue	[100 50 50]	17.8	**2.39**	4.92	29.6	8.38	**4.88**
	[50 100 50]	21.8	**6.52**	7.66	35.6	15.4	**13.6**
	[50 50 100]	8.88	**4.67**	8.92	12.8	3.59	**2.51**

T_{90}, and T_{60} can be represented by summing the pixel-wise difference deviated from T_i. That is, the lower the sum of squared error, the better the quality. A general representation of the error is as follows:

$$E = \sum_{x,y} |T_t(x,y) - T_i(x,y)|^2, \qquad T_t \in \{T_o, T_{90}, T_{60}\}. \tag{26}$$

We choose a representative set of test images and the screen colors and adopt red, green, and blue as the primary colors. We use three uniform-colored images as test images and set their pixel value [R G B] to [100 50 50], [50 100 50] and [50 50 100], respectively. They are paired with red, green and blue screens to form nine combinations, covering the basis of all possible image-screen pairing in this setup.

Table 2 lists the results in sum of squared error. There are two key observations. First, it is evident that, though 90 deg compensation performs better when seen at 90 deg, it is outperformed by 60 deg compensation when the viewing angle is changed to 60 deg. The result strongly indicates that the radiometric compensation should be adaptive to the viewer's position. More importantly, our algorithm is able to further lower the error. Second, the quality of the original image is further worsened when seen from 60 deg. This can be explained by considering the following two factors that affect the projection: specular light and the screen color. The perceived quality at 90 deg tends to incorporate large portion of specular light, which is of the same color of the original image. However, when seen from 60 deg, the specular light dwindles, and the influence from the screen color increases, leading to greater photometric distortion. The worsened quality implies the necessity for radiometric compensation being used under such condition.

5.2 *Subjective Evaluation*

We took a total of 26 images in the Kodak lossless true color image suite[41] as the test images. We recruited 20 volunteers to judge the quality of the projections. Among them, 13 were male and seven were female, with their age ranging from 22 to 27. All subjects reported no severe visual abnormalities other than myopia.

Each test image was projected onto a magenta screen with three variations: (1) the original image T_o; (2) the 90 deg compensated image T_{90}; and (3) the 60 deg compensated image T_{60}. For each test image, the projection process consisted of three rounds, and in each round two of the three candidates (T_o, T_{90}, and T_{60}) were projected. Actually, it was a round-robin contest for T_o, T_{90}, and T_{60} in a random order. The subjects were asked to select from the two candidates the one with better quality. The criteria for judging the quality included chroma correctness, brightness, and contrast. The voting system was implemented using MATLAB, where the subject used keyboard to cast the vote. The same process was repeated twice, where the subject viewed the projection at 60 deg in the first time and 90 deg in the second.

Figure 14 summarizes the result of each match. Figure 14(a) to 14(c) are for subjects being at 90 deg viewing angle, while Fig. 14(d) through 14(f) are for 60 deg. The overall statistics of each match is shown in the bottom-right box. Here, we use the symbol ">" to denote quality superiority. For instance, by "$x > y$" we mean "candidate x has better quality than candidate y." We now discuss the result of each match: $\{T_o, T_{90}\}$, $\{T_o, T_{60}\}$, and $\{T_{90}, T_{60}\}$ as follows.

$\{T_o, T_{90}\}$: This match evaluates the effectiveness of the conventional radiometric compensation technique. When seen at 90 deg [Fig. 14(a)], T_{90} is highly preferred (90.19%) over T_o, indicating that the radiometric compensation is successful. It seems counterintuitive that, when seen at 60 deg, T_{90} performs even better as it received 98.85% of the votes. This can be explained by noting that the quality of T_o severely worsens when the viewing angle changes from 90 to 60 deg, making it even less competitive. As the specular light abounding at 90 deg become out of sight when seen at 60 deg, the screen color gradually dominates, and hence ruins, the quality of T_o. For this reason, one should not mistakenly consider that the conventional technique also performs well for T_{90} when seen at 60 deg, although T_{90} received more votes in 60 deg (98.85%) than in 90 deg (90.19%).

$\{T_o, T_{60}\}$: This match shows that T_{60} received votes as high as 97.69% against T_o, indicating that T_{60} has great quality when seen at 60 deg [see Fig. 14(e)]. The match also shows that, though highly preferred at 60 deg, T_{60} was considered poor in quality (only 62.88% votes) when seen at 90 deg. This is in accordance with our expectation: The amount of compensation in T_{60} exceeds what is needed for 90 deg viewing angle so that the specular highlight of the compensated color reflects and, as a result, spoils the visual quality. When viewing a magenta screen at 90 deg, for example, strong green color in T_{60} would mostly be reflected as specular light. Consequently, the resulting image is perceived much greener than the original image. In this case, subjects showed no strong preference over either T_o or T_{60}.

$\{T_{90}, T_{60}\}$: This is the key part of the whole evaluation, which proves the validity of the proposed algorithm. From Fig. 14(f) we can see that T_{60}, generated by the proposed method, outperforms T_{90} when seen at 60 deg. Recall that the traditional radiometric compensation schemes do not

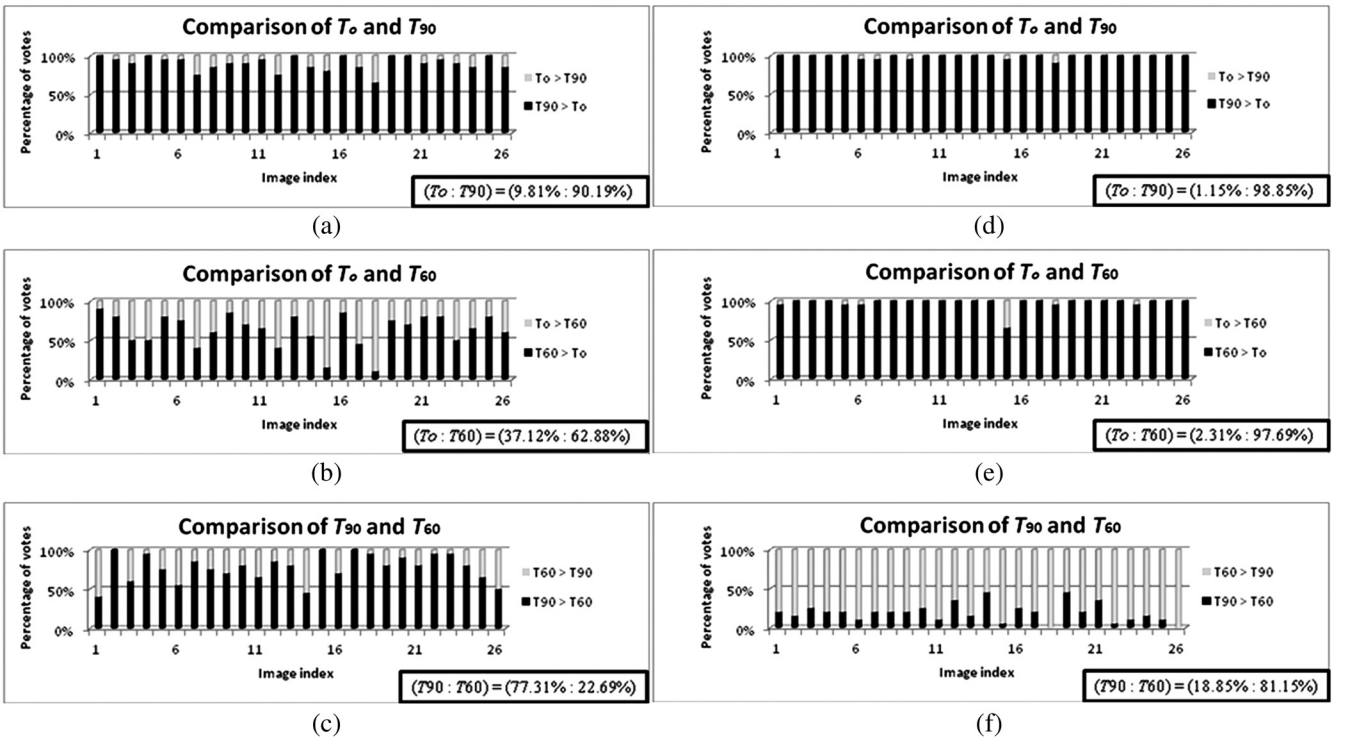

Fig. 14 Statistics of the subjective evaluation. By "*x* > *y*" we mean that "*x* has better quality than *y*." For (a), (b), and (c), the subject views the projection at 90 deg viewing angle. For (d), (e), and (f), the viewing angle is 60 deg. The statistics of total votes are shown in the bottom-right box of each subfigure.

take specular light and viewing angle into account. In contrast, our technique is able to provide better visual quality. Figure 13(c) and 13(f) together strongly suggest that the radiometric compensation should be adaptive to the viewing angle. In other words, it is not the best practice to apply a one-for-all compensation and ignore the viewing direction. A view-dependent compensation works much better.

6 Conclusion

In this paper, we have addressed the problem of recovering the projection quality for non-Lambertian surfaces. We have proposed a novel specular highlight estimation algorithm for radiometric compensation and discussed how calibration images for different viewing angles can be predicted from the reconstructed specular light model.

The proposed algorithm has been rigorously tested. Both objective and subjective evaluations have been carried out on a number of test images, and it is shown that the proposed algorithm consistently outperforms conventional ones. The proposed technique provides good visual quality for the projection. In addition, due to its low complexity, it can be easily incorporated into existing procam systems.

Acknowledgments

This project is supported in part by a grant from the National Science Council of Taiwan under Contract NSC 100-2221-E-002-197-MY3, a grant from National Taiwan University under Contract 102R7609-2, and a grant from the Himax Technologies, Inc.

References

1. S. Zollmann, T. Langlotz, and O. Bimber, "Passive-active geometric calibration for view-dependent projections onto arbitrary surfaces," *J. Virtual Reality Broadcast.* **4**(6), 1–10 (2007).
2. J. Oh et al., "Portable projection-based AR system," in *Proc. 3rd Int. Conf. on Adv. in Vis. Comput.*, pp. 742–750, Springer-Verlag, Berlin, Heidelberg (2007).
3. H. Park et al., "Surface-independent direct-projected augmented reality," in *Proc. 7th Asian Conf. Comput. Vision*, pp. 892–901, Springer-Verlag, Berlin, Heidelberg (2006).
4. T. Johnson and H. Fuchs, "Real-time projector tracking on complex geometry using ordinary imagery," in *Proc. IEEE Conf. Comput. Vis. and Pattern Recognit.*, pp. 1–8, IEEE Computer Society, Washington, DC (2007).
5. E. S. Bhasker, R. Juang, and A. Majumder, "Registration techniques for using imperfect and partially calibrated devices in planar multi-projector displays," *IEEE Trans. Visual. Comput. Graph.* **13**(6), 1368–1375 (2007).
6. M. Brown, A. Majumder, and R. Yang, "Camera based calibration techniques for seamless multi-projector displays," *IEEE Trans. Visual. Comput. Graph.* **11**(2), 193–206 (2005).
7. R. Raskar et al., "RFIG lamps: interacting with a self-describing world via photosensing wireless tags and projectors," in *Proc. ACM SIGGRAPH*, pp. 406–415, ACM, New York, NY (2004).
8. J. Salvi, J. Pages, and J. Batlle, "Pattern codification strategies in structured light systems," *Pattern Recognit.* **37**(4), 827–849 (2004).
9. R. Yang and G. Welch, "Automatic and continuous projector display surface calibration using every-day imagery," in *Proc. Int. Conf. in Central Europe on Comput. Graph., Visual. and Comput. Vis.*, Union Agency, Plzen, Czech Republic (2001).
10. R. Raskar, "Oblique projector rendering on planar surfaces for a tracked user," in *ACM SIGGRAPH Conf. Abstr. Appl.*, pp. 260, ACM, New York, NY (1999).
11. T. H. Huang, C. T. Kao, and H. H. Chen, "Quality enhancement of a procam system by radiometric compensation," to appear in *Proc. 14th IEEE Int. Workshop on Multimedia Signal Process.*, pp. 192–197, IEEE Computer Society, Washington, DC (2012).
12. D. C. Kim et al., "Color correction for projected image on colored screen based on a camera," *Proc. SPIE* **7866**, 786606 (2011), .
13. M. H. Lee, H. Park, and J. I. Park, "Fast radiometric compensation accomplished by eliminating color mixing between projector and camera," *IEEE Trans. Consumer Electron.* **54**(3), 987–991 (2008).

14. S. Zollmann and O. Bimber, "Imperceptible calibration for radiometric compensation," in *Proce. Eurograph.*, pp. 61–64, EUROGRAPHICS Association, Goslar, Germany (2007).
15. G. Wetzstein and O. Bimber, "Radiometric compensation through inverse light transport," in *Proc. Pacific Conf. Comput. Graph. and Appl.*, pp. 391–399, IEEE Computer Society, Washington, DC (2007).
16. A. Grundhofer et al., "Dynamic adaptation of projected imperceptible codes," in *Proc. IEEE/ACM Int. Sym. on Mixed Augmented Reality*, pp. 1–10, IEEE Computer Society, Washington, DC (2007).
17. O. Bimber, A. Emmerling, and T. Klemmer, "Embedded entertainment with smart projectors," *J. Comps.* **38**(1), 48–55 (2005).
18. K. Fujii, M. D. Grossberg, and S. K. Nayar, "A projector-camera system with real-time photometric adaptation for dynamic environments," in *Proc. IEEE Conf. Comput. Vision and Pattern Recognit.*, Vol. 1, pp. 814–821, IEEE Computer Society, Washington, DC (2005).
19. T. P. Koninckx et al., "Scene-adapted structured light," in *Proc. IEEE Conf. Comput. Vis. and Pattern Recognit.*, pp. 611–618, IEEE Computer Society, Washington, DC (2005).
20. O. Bimber et al., "Enabling view-dependent stereoscopic projection in real environments," in *Proc. IEEE/ACM Int. Sym. on Mixed Augmented Reality*, pp. 14–23, IEEE Computer Society, Washington, DC (2005).
21. M. D. Grossberg et al., "Making one object look like another: controlling appearance using a projector-camera system," in *Proc. IEEE Conf. Comput. Vis. and Pattern Recognit.*, Vol. 1, pp. I-452–I-459, IEEE Computer Society, Washington, DC (2004).
22. S. K. Nayar et al., "A projection system with radiometric compensation for screen imperfections," in *IEEE Int. Workshop on Projector-Camera Systems*, IEEE Computer Society, Washington, DC (2003).
23. T. Yoshida, C. Horii, and K. Sato, "A virtual colour reconstruction system for real heritage with light projection," in *Proc. Int. Conf. Virtual Systems and Multimedia*, pp. 161–168 (2003).
24. D. Caspi, N. Kiryati, and J. Shamir, "Range imaging with adaptive colour structured light," *IEEE Trans. Pattern Anal. Mach. Intell.* **20**(5), 470–480 (1998).
25. A. Grundhoefer and O. Bimber, "Real-time adaptive radiometric compensation," *Trans. Visual. Comput. Graph.* **14**(1), 97–108 (2008).
26. H. Park et al., "Contrast enhancement in direct-projected augmented reality," in *IEEE Int. Conf. Multimedia and Expo*, pp. 1313–1316, IEEE Computer Society, Washington, DC (2006).
27. D. Wang et al., "Radiometric compensation in a projector-camera system based on the properties of human vision system," in *Proc. IEEE Conf. Comput. Vis. and Pattern Recognit.*, pp. 100, IEEE Computer Society, Washington, DC (2005).
28. M. Ashdown et al., "Perceptual photometric compensation for projected images," *IEICE Trans. Inf. Sys.* **J90-D**(8), 2115–2125 (2007).
29. M. Ashdown et al., "Robust content-dependent photometric projector compensation," in *Proc. IEEE Conf. Comput. Vision and Pattern Recognit. Workshop*, pp. 6, IEEE Computer Society, Washington, DC (2006).
30. O. Bimber et al., "The visual computing of projector-camera systems," in *ACM SIGGRAPH*, pp. 84-1–84-25, ACM, New York, NY (2008).
31. H. Park et al., "Radiometrically-compensated projection onto non-Lambertian surface using multiple overlapping projectors," in *Proc. Pacific-Rim Conf. Adv. in Image and Video Technol.*, pp. 534–544, Springer-Verlag, Berlin, Heidelberg (2006).
32. H. Park et al., "Specularity-free projection on nonplanar surface," in *Proc. Pacific-Rim Conf. Multimedia*, pp. 606–616, Springer-Verlag, Berlin, Heidelberg (2005).
33. H. Park et al., "Specular reflection elimination for projection-based augmented reality," in *Proc. IEEE/ACM Int. Sym. Mixed Augmented Reality*, pp. 194–195, IEEE Computer Society, Washington, DC (2005).
34. E. A. Merritt and M. E. P. Murphy, "A program for photorealistic molecular graphics," *Acta Crystallograph. D* **50**(6), 869–873 (1994).
35. C. M. Goral et al., "Modeling the interaction of light between diffuse surfaces," in *Proc. Conf. Comput. Graph. and Interactive Tech.*, pp. 213–222, ACM, New York, NY (1984).
36. R. L. Cook and K. E. Torrance, "A reflectance model for Comp. graphics," in *Proc. Conf. Comput. Graph. and Interactive Tech.*, pp. 307–316, ACM, New York, NY (1981).
37. J. F. Blinn, "Models of light reflection for Comp. synthesized pictures," *SIGGRAPH Comp. Graph.* **11**(2), 192–198 (1977).
38. B. T. Phong, "Illumination for Comp. generated pictures," *Commun. ACM* **18**(6), 311–317 (1975).
39. A. S. Glassner, *An Introduction to Ray Tracing*, Academic Press, Waltham, MA (1989).
40. R. Franzen, "Kodak Lossless True Color Image Suite," (30 October 2012), http://r0k.us/graphics/kodak/ (06 January 2013).
41. Z. Zhang, "Flexible camera calibration by viewing a plane from unknown orientations," in *Proc. 7th IEEE Int. Conf. on Comput. Vis.*, Vol. 1, pp. 666–673, IEEE Computer Society, Washington, DC (1999).

Chen-Tai Kao received a BS degree in electrical engineering from National Taiwan University in 2012. He is currently working toward an MS degree at the Graduate Institute of Communication Engineering, National Taiwan University. His research interests are in the area of perceptual-based image processing.

Tai-Hsiang Huang received his BS degree in electrical engineering from National Taiwan University in 2006. He is currently working toward a PhD degree at the Graduate Institute of Communication Engineering, National Taiwan University. His research interests are in the area of perceptual-based image and video processing.

Hua Lee prior to his return to UCSB in 1990, he was on the faculty of the University of Illinois at Urbana-Champaign. His research interests cover the areas of imaging system optimization, high-performance image formation algorithms, synthetic-aperture radar and sonar systems, acoustic microscopy, microwave nondestructive evaluation, and dynamic vision systems. His research laboratory was the first to produce the holographic and tomographic reconstructions from a scanning laser acoustic microscope, and his research team is also known as the leader in pulse-echo microwave nondestructive evaluation of civil structures and materials.

Homer H. Chen received a PhD degree in electrical and computer engineering from University of Illinois at Urbana-Champaign. Since August 2003, he has been with the College of Electrical Engineering and Computer Science, National Taiwan University, where he is Irving T. Ho chair professor. Prior to that, he held various R&D management and engineering positions with U.S. companies over a period of 17 years, including AT&T Bell Labs, Rockwell Science Center, iVast, and Digital Island (acquired by Cable & Wireless). He was a US delegate for ISO and ITU standards committees and contributed to the development of many new interactive multimedia technologies that are now part of the MPEG-4 and JPEG-2000 standards. His professional interests lie in the broad area of multimedia signal processing and communications. He is an IEEE Fellow. He was an associate editor of *IEEE Transactions on Circuits and Systems for Video Technology* from 2004 to 2010, *IEEE Transactions on Image Processing* from 1992 to 1994, and *Pattern Recognition* from 1989 to 1999. He served as a guest editor for *IEEE Transactions on Circuits and Systems for Video Technology* in 1999 and *IEEE Transactions on Multimedia* in 2011.